



## City Research Online

### City, University of London Institutional Repository

---

**Citation:** Nazeer, Y. H., Ehmann, M, Sami, M and Gavaises, E. ORCID: 0000-0003-0874-8534 (2020). Atomization Mechanism of Internally Mixing Twin-Fluid Y-Jet 1 Atomizer. Journal of Energy Engineering,

This is the accepted version of the paper.

This version of the publication may differ from the final published version.

---

**Permanent repository link:** <https://openaccess.city.ac.uk/id/eprint/24687/>

**Link to published version:**

**Copyright and reuse:** City Research Online aims to make research outputs of City, University of London available to a wider audience. Copyright and Moral Rights remain with the author(s) and/or copyright holders. URLs from City Research Online may be freely distributed and linked to.

---

City Research Online:

<http://openaccess.city.ac.uk/>

[publications@city.ac.uk](mailto:publications@city.ac.uk)

---

# Atomization Mechanism of Internally Mixing Twin-Fluid Y-Jet Atomizer

Y. H. Nazeer<sup>1\*</sup>, M. Ehmann<sup>1</sup>, M. Sami<sup>2</sup>, M. Gavaises<sup>3</sup>

<sup>1</sup>Mitsubishi Hitachi Power Systems Europe GmbH, Germany

<sup>2</sup>ANSYS, Inc., Houston, Texas, USA

<sup>3</sup>School of Mathematics, Computer Sciences and Engineering, City, University of London, UK

## Abstract

The atomization mechanism of the gas-liquid multiphase flow through internally mixing twin-fluid Y-jet atomizer has been studied by examining both the internal and external flow patterns. Superheated steam and Light Fuel Oil (LFO) are used as working fluids. The flow is numerically modeled using the compressible Navier-Stokes equations; hybrid Large Eddy Simulation approach through Wall Modeled Large Eddy Simulations (WMLES) is used to resolve the turbulence with the Large Eddy Simulations, whereas the Prandtl Mixing Length Model is used for modeling the subgrid-scale structures, which are affected by operational parameters. VOF-to-DPM transition mechanism is utilized along with dynamic solution-adaptive mesh refinement to predict the initial development and fragmentation of the gas-liquid interface through Volume-of-Fluid (VOF) formulations on a sufficiently fine mesh, while Discrete Phase Model (DPM) is used to predict the dispersed part of the spray on the coarser grid. Two operational parameters, namely gas-to-liquid mass flow rate ratio (GLR) and liquid-to-gas momentum ratio are compared; the latter is found to be an appropriate operational parameter to describe both the internal flow and atomization characteristics. It is confirmed that the variation in the flow patterns within the mixing-port of the atomizer coincides with the variation of the spatial distribution of the spray drops.

Keywords: Internally Mixing Twin-Fluid Y-Jet Atomizer, VOF-to-DPM, Wall Modeled Large Eddy Simulations (WMLES)

## Nomenclature

### Acronyms

SMD	Sauter Mean Diameter
VOF	Volume of Fluid
HPC	High-Performance Computing
WMLES	Wall Modeled Large Eddy Simulations
LES	Large Eddy Simulations
RANS	Reynolds-Averaged Navier-Stokes
DPM	Discrete Phase Model
SGS	Subgrid Scale
Eq.	Equation
HPC	High Performance Computing

### Subscripts

$p$	Phase $p$
$q$	Phase $q$
$m$	Mixing Port
$M$	Mixing Point
$g$	Gas
$l$	Liquid
$pz$	Premix Zone
$r$	relative
$pr$	Particle
$max$	Maximum

$min$	Minimum
Superscript	
$T$	Transpose
$s$	Sub-grid Scale
Symbols	
$\alpha$	Volume Fraction
$\rho$	Density, $kg/m^3$
$V$	Velocity, $m/s$
$P$	Pressure, Pa
$\mu$	Viscosity, $kg/m.s$
$g$	Gravitational Acceleration, $m/s^2$
$T_\sigma$	Surface Tension Force, $N$
$T$	Temperature, $K$
$k$	Curvature, $m^{-1}$
$\sigma$	Surface Tension, $N/m$
$E$	Energy, $J$
$K_\infty$	Thermal Conductivity, $W/m.K$
$K_{eff}$	Effective Thermal Conductivity, $W/m.K$
$\Delta$	Modified Length Scale, $m$
$\tau_{ij}$	Viscous Stress, $N/m^2$
$\nu_t$	Eddy Viscosity, $m^2/s$
$\delta_{ij}$	Kronecker Delta
$y^+$	Dimensionless Wall Distance
$\Omega$	Vorticity, $s^{-1}$

$S$	Strain Rate, $s^{-1}$
$\theta$	Angle, $^{\circ}$
$l$	Length, $mm$
$d$	Diameter, $m$
$\tau_{kkk}$	Isotropic Part of the Subgrid Stress, $N/m^2$
$\varphi$	Momentum Ratio
$M$	Mass Flow Rate, $kg/s$
$G$	Mass Velocity, $kg/m^2s$
$C_w$	Empirical Constant
$h_{max}$	Maximum Edge Length, $m$
$h_{wn}$	Grid Step in Wall Normal Direction, $m$
$d_w$	Distance from Wall, $m$
$C_{smag}$	Smagorinsky Constant
$a_1$	Constant defined in Eq. 11
$a_2$	Constant defined in Eq. 11
$a_3$	Constant defined in Eq. 11
$C_D$	Drag Coefficient
$F_D$	Drag Force Per Unit Mass, $N/kg$
$Ar$	Surface Area, $m^2$
$h$	Convective Heat Transfer Coefficient, $W/Km^2$
$Y$	Coordinate Axis
$C$	Heat Capacity, $J/K$

26

27

28

## 29 Introduction

30 The description of “twin-fluid atomizer” can be applied to any nozzle in which the driving force for  
31 the liquid jet break up is air, steam or any gas. Twin-fluid atomizers could be classified into “air-  
32 assist,” “airblast” and “effervescent” atomizers (Lefebvre, 1992). One thing common between  
33 different types of twin-fluid air-assist atomizers (Mlkvik, et al., 2015), (Pacifico & Yanagihara, 2014)  
34 and (Kufferath, et al., 1999) and airblast atomizers (Inamura, et al., 2019), (Okabe, et al., 2019) and  
35 (Roudini & Wozniak, 2018) is that the bulk liquid to be atomized is first transformed into a jet or  
36 sheet before being exposed to high-velocity gas. In contrast, in effervescent atomizers (Roesler &  
37 Lefebvre, 1989), (Buckner, et al., 1990a), (Buckner, et al., 1990b) and (Sovani, et al., 2001) the  
38 atomizing gas is injected into the bulk liquid at low velocity to form a bubbly two-phase mixture  
39 upstream of the discharge orifice. The main difference between the air-assist and airblast atomizers  
40 is that the former employs high pressure source of air or steam at very high velocities (usually sonic)  
41 and at relatively smaller mass flow rates while the latter employ low pressure gas source and much  
42 larger amount of gas flow at relatively lower velocities (Lefebvre, 1992) and (Lefebvre, 1980).

43 Air-assist atomizers can be classified into internal-mixing and external-mixing types. In the former,  
44 high velocity air or steam impinges on the liquid jet within the mixing chamber of the nozzle while in  
45 the latter the air or steam impinges on the liquid sheet or jet outside the discharge orifice. In the  
46 external mixing type, the spray cone angle is minimum for the maximum gas flow, and the spray  
47 widens as the gas flow is reduced; whereas external mixing type can be designed to give constant  
48 spray angle at all liquid flow rates. Internal mixing air-assist atomizers are highly suitable for high  
49 viscous liquids, as good atomization can be achieved down to very low liquid mass flow rates  
50 (Barreras, et al., 2008).

51 In large oil-fired industrial boilers or thermal power plants, either Y-jet atomizers or internal mixing  
52 chamber twin-fluid atomizers are used (Barreras, et al., 2006). The former is usually used with light  
53 fuel oil while the latter is used with heavy fuel oil and steam as auxiliary fluid (Li, et al., 2012). The

54 characteristics of the Y-jet atomizer is that the liquid and gas (air or steam) are mixed before injected  
55 out. It generally consists of a number of jets, from a minimum of two to maximum of 20, arranged  
56 annularly to provide a hollow conical spray. In each individual 'Y', oil is injected into the mixing port,  
57 where it mixes with the atomizing fluid (steam or air) admitted through the gas port. The mixing  
58 ports are uniformly spaced around the atomizer body at an angle to the nozzle axis (see Figure 1) so  
59 that the individual jets of two-phase mixture emanating from the mixing ports rapidly merge to form  
60 a hollow conical spray.

61 The spraying performance (expressed by the mean droplet size) of the Y-jet atomizer is reported to  
62 be affected by properties of gas and liquid, injection pressure, and also by the geometric  
63 configurations such as the mixing-port size and the intersecting angle between the liquid and gas  
64 ports. Mullinger and Chigier (Mullinger & Chigier, 1974) and Prasad (Prasad, 1982) studied the effect  
65 of geometric parameters on the mean drop size and suggested the design criteria to generate the  
66 fine droplets. Song and Lee (Song & Lee, 1994) conducted the experimental examination, with water  
67 and air as test fluids, to study the effect of mixing port length on the Y-jet atomizer's spray  
68 performance. They concluded that the mean droplet size decreases and becomes spatially even as  
69 the mixing port length is reduced. In a classical study, with water and air as working fluids, Song and  
70 Lee (Song & Lee, 1996) studied the atomization mechanism of the gas-liquid mixture flowing through  
71 internally mixing twin-fluid Y-jet atomizer by examining both the internal and external nozzle flow  
72 patterns. They compared two operational parameters, namely gas-to-liquid mass flow rate ratio  
73 (GLR) and liquid-to-gas momentum ratio to describe the internal flow patterns and external drop size  
74 distribution. The atomization model of Y-jet atomizer proposed by Mullinger and Chigier (Mullinger &  
75 Chigier, 1974), Song and Lee (Song & Lee, 1996) and Andreussi et al. (Andreussi, et al., 1992) is  
76 almost the same. The main difference is that the internal atomization mechanism proposed by Song  
77 and Lee is subdivided into two parts namely direct collision mode and entrainment/deposition mode.

78

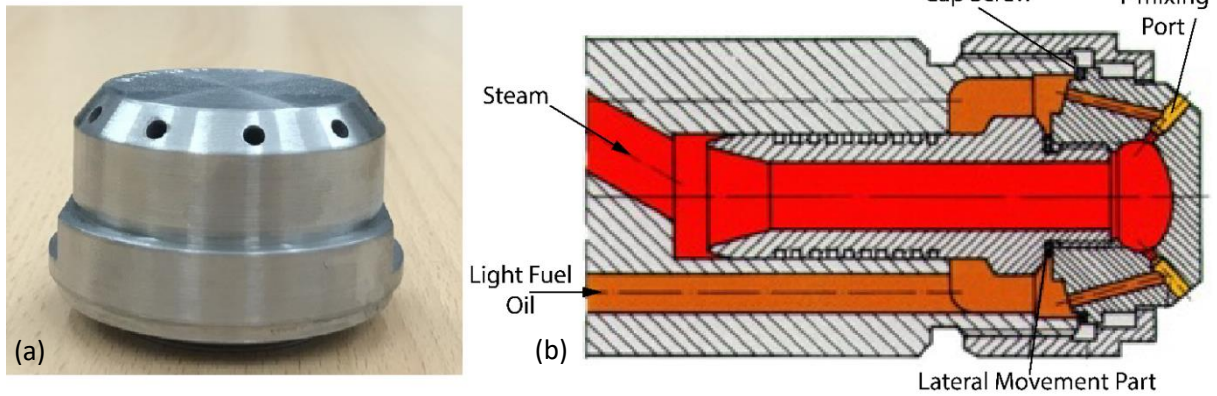
79

80

81

82

83



84 **Figure 1** (a) Nozzle head of twin fluid Y-jet atomizer (b) Schematic of internally mixing twin-fluid Y-jet atomizer.

85 There are few studies predicting the internal flow characteristics, flow rates and energy required for  
86 the atomization (Nazeer, et al., 2019), (De Michele, et al., 1991), (Andreussi, et al., 1994), (Andreussi,  
87 et al., 1992) and (Song & Lee, 1994). There also exist several studies on the atomization  
88 characteristics of twin-fluid Y-jet atomizers (Song & Lee, 1996), (Mullinger & Chigier, 1974), (Neya, et  
89 al., 1975), and (Andreussi, et al., 1994); parameters such as atomizer geometry and injection  
90 conditions were taken as “input” and the spray performance was considered as “output.” However,  
91 the effect of internal flow conditions on the atomization characteristics is not reported in detail. The  
92 effect of internal flow condition can be understood only by looking into both the internal flow  
93 patterns and the atomization mechanism simultaneously. (Neya, et al., 1975), (Andreussi, et al.,  
94 1994) and (Song & Lee, 1996) are the only cases paying attention to the effect of internal flow  
95 pattern on the atomization. However, the results are restricted to simplified conditions and  
96 geometry, and water and air as working fluids.

97 A broad range of time and length scales are involved in atomization; thus, approximations and  
98 modeling of unresolved sub-grid scale phenomena become inevitable in CFD of such multiphase flow  
99 phenomena (Li, et al., 2020). The numerical simulation of the liquid spray generation often aims in  
100 predicting drop size distribution, spray penetration length and spray cone angle (Zhou, et al., 2019 a)  
101 and (Zhou, et al., 2019 b). Since the liquid spends most of its residence time in the form of droplets,  
102 simulation methodologies for the dispersed multiphase flow are usually utilized. The two widely



103 implemented approaches used for the description of the dispersed phase are the Eulerian-Eulerian  
104 and Eulerian-Lagrangian.

105 The Eulerian-Eulerian multiphase approach describes the motion of the dispersed phase by the same  
106 means as the continuous phase, i.e. a set of Navier-Stokes equations for the continuity and  
107 momentum transport, potentially along with transport equations for energy and other conserved  
108 quantities. The gas-liquid interface can be tracked by an additional transport equation such as the  
109 widely used VOF method (Hirt & Nichlos, 1981) or similar and early applications to internal nozzle  
110 flow and atomization (Arcoumanis, et al., 1999) and (Gavaises & Arcoumanis, 2001). Such methods  
111 requires much smaller time steps and much higher mesh resolutions than diffuse interface  
112 approaches and Eulerian-Lagrangian methods, as the computational mesh around the phase  
113 boundary of each droplet must be refined enough to adequately resolve. The volume displacement is  
114 inherently accounted for, which can be important for the dense part of the spray. However, this  
115 method is prohibitive in terms of computational expenses and requires large HPC resources.

116 In Eulerian-Lagrangian multiphase approaches (Jiang, et al., 2010), referred to as Discrete Particle  
117 Methods (DPM), the gas/carrier phase is still represented by solving the governing equation of the  
118 flow but the liquid phase is represented by a number of discrete computational particles, which are  
119 tracked through the domain by solving the particle's equation of motion. Particle tracker use physical  
120 properties of individual droplets in order to account for the exchange of mass, momentum and  
121 energy etc. with the continuous phase. This approach is relatively inexpensive since it allows the  
122 mesh to be coarser than the size of the droplets. However, the gas volume displacement is usually  
123 ignored; this may affect the solution's accuracy, hence these so-called dense models have been  
124 developed (Tonini, et al., 2008). Furthermore, in the regions where spray does not consist of discrete  
125 spherical droplets, special models must be employed to predict the primary breakup of the initial  
126 contiguous jet.

127 ANSYS Fluent provides the capability to combine the above mentioned two approaches through VOF-  
128 to-DPM transition mechanism. The initial jet and its primary breakup are predicted using VOF  
129 formulations on sufficiently fine mesh, while the resulting dispersed part of the spray is predicted by  
130 the DPM. The ELSA model (Vallet, et al., 2001) and (Nykteri, et al., 2020) is another alternative  
131 approach that provides a dynamic transition between an Eulerian and a Lagrangian framework in the  
132 primary and secondary liquid spray atomization regions, respectively. The hybrid VOF-to-DPM model  
133 automatically finds the liquid lumps detached from the liquid core in the VOF solution. It then checks  
134 for their eligibility for the VOF-to-DPM model transition against the user specified criteria of the lump  
135 size and asphericity. If a liquid lump satisfies the criteria, the liquid lump is removed from VOF solver  
136 and converted to a point mass in the Lagrangian formulations. Converting liquid lumps to Lagrangian  
137 formulation does not impose volume displacement on the continuous phase VOF flow simulations. In  
138 order to circumvent spurious momentum sources, a volume of a gas with the same volume as the  
139 liquid lump is created in the VOF simulation to maintain the volume conservation. The hybrid VOF-to-  
140 DPM model is validated against the experimental studies to determine the Sauter mean diameter  
141 (SMD) drop size distribution for a liquid jet in air cross-flow (Schitze, et al., 2018) and (Sami, et al.,  
142 2019) and also the reverse transition mechanism i.e. DPM-to-VOF is reported to agree well with the  
143 experimental studies to determine the film formation from the drops (Kumar, et al., 2018).

144 In the present study, the multiphase flow through the internally mixing twin-fluid Y-jet atomizer is  
145 numerically modelled to determine the internal flow behavior and the subsequent atomization  
146 mechanism. It is the first numerical study to report the atomization mechanism of the internally  
147 mixing twin-fluid Y-jet atomizer. The influence of two dimensionless operating parameters, namely  
148 gas-to-liquid mass flow rate ratio and liquid-to-gas momentum ratio are compared; the latter is  
149 found to be more appropriate dimensionless parameter to describe the internal flow behavior and  
150 the atomization characteristics, as it defines to a large extent the liquid and gas distribution inside  
151 the atomizer, which then affects the near-nozzle atomization and the distribution of the formed  
152 ligaments and droplets. It should be also mentioned that although more sophisticated atomization

153 models exist in the literature for the fragmentation of liquids, the applied model has been validated  
154 from the author's group for other flow conditions, like for example the secondary break-up of liquid  
155 droplets (Stefanitsis, et al., 2019a), (Stefanitsis, et al., 2019b), (Strotos, et al., 2018), (Strotos, et al.,  
156 2016a), (Strotos, et al., 2016b) and (Strotos, et al., 2011). For the specific conditions simulated here,  
157 the complexity of the flow within the atomizer, it is unfortunate that quantitative experimental data  
158 for the atomizing spray that would be needed for quantitative validation of the applied  
159 computational models do not exist.

160 Following, the computational model utilized and the geometry and operating conditions are  
161 described, followed by the presentation of the results; these include initially the flow structure inside  
162 the atomizer and then its influence on the spray formation; the most important conclusions are  
163 summarized at the end.

## 164 Numerical Method

165 VOF

166 The compressible Navier-Stokes equations are numerically solved using the finite volume  
167 approximation; the Volume of Fluid (VOF) technique with Geometric Reconstruction Scheme is  
168 employed in ANSYS Fluent with a time step of  $10^{-8}$  to model the gas-liquid interface. The interface is  
169 modeled as interpenetrating media; the two phases are sharing same properties while the bulk  
170 properties of the individual phase are scaled according to the cell's volume fraction which varies  
171 between zero and one.

172 The corresponding transport equations that consider the volume fraction in the cell, with  $\rho_q$   
173 representing the density and  $\vec{V}_q$  the velocity vector of the  $q^{th}$  phase, are:

$$\frac{d}{dt}(\alpha_q \rho_q) + \nabla \cdot (\alpha_q \rho_q \vec{V}_q) = 0 \quad (1)$$

174 The single set of momentum equation is shared among the phases based on mixture properties.

$$\frac{d}{dt}(\rho\vec{V}) + \nabla \cdot (\rho\vec{V}\vec{V}) = -\nabla P + \nabla \cdot [\mu(\nabla\vec{V} + \nabla\vec{V}^T)] + \rho\vec{g} + \vec{T}_\sigma \quad (2)$$

175

176 Where density is defined as:  $\rho = \sum \alpha_q \rho_q$ , viscosity as:  $\mu = \sum \mu_q \alpha_q$ , and velocity as:  $\vec{V} =$

177  $\frac{1}{\rho} \sum_{q=1}^n \alpha_q \rho_q \vec{V}_q$   $\vec{T}_\sigma$  is the volumetric force source term arising due to the surface tension. It is

178 modelled by continuum surface force model proposed by Brackbill et al. (Brackbill, et al., 1992). This

179 model treats the surface tension as the pressure jump across the interface. The forces at the surface

180 are expressed as volume forces using the divergence theorem:

$$T_\sigma = \sum_{pairs,p,q} \sigma_{p,q} \frac{\alpha_p \rho_p k_q \nabla \alpha_q + \alpha_q \rho_q k_p \nabla \alpha_p}{\frac{1}{2}(\rho_p + \rho_q)} \quad (3)$$

181

182 The curvature of one surface is negative of other,  $k_p = -k_q$  and divergence of the volume fraction is

183 negative of other  $\nabla \alpha_p = -\nabla \alpha_q$ . This simplifies the equation to:

$$T_\sigma = \sigma_{p,q} \frac{\rho k_p \nabla \alpha_p}{\frac{1}{2}(\rho_p + \rho_q)} \quad (4)$$

184 The total energy of the flow is modelled by following equation.

$$\frac{d}{dt}(\rho E) + \nabla \cdot (\vec{V}(\rho E + P)) = \nabla \cdot (K_{eff} \nabla T + \bar{\tau} \cdot \vec{V}) \quad (5)$$

185

186 Here  $K_{eff}$  is effective thermal conductivity,  $\bar{\tau}$  is the viscous stress tensor; the energy  $E$  and

187 temperature  $T$  are mass averaged variables.

$$E = \frac{\sum_{q=1}^n \alpha_q \rho_q E_q}{\sum_{q=1}^n \alpha_q \rho_q} \quad (6)$$

188

189  $E_q$  is the internal energy of each phase; both phases share the same temperature.

190 Transition

191 Asphericity is the shape base criterion used by VOF-to-DPM model to identify the liquid lumps which  
 192 can be converted from resolved liquid using VOF model to particles tracked with the DPM model. Its  
 193 value is zero for a perfect sphere. Asphericity values of the liquid lumps are determined in two ways,  
 194 namely calculated from normalized radius standard deviation and radius-surface orthogonality. In  
 195 the first method, for every facet of the liquid lump surface, the distance between the facet center  
 196 and the lump center of gravity is calculated and then normalized by the average radius. In the second  
 197 method, for every facet of the liquid lump surface, a vector from the lump's center of gravity to the  
 198 center of the lump boundary facet is computed and then used in a dot product with the facet unit  
 199 normal vector. Only lumps for which the asphericity values calculated from both methods are below  
 200 the user-specified maximum asphericity values are selected for transition from VOF liquid to DPM  
 201 particles.

202 DPM

203 The trajectory of the discrete phase is predicted by integrating the force balance on the particle. The  
 204 force balance equation, which is written in a Lagrangian reference frame, equates the particle inertia  
 205 with the force acting on the particle. It can be written as:

$$\frac{d\vec{V}_{pr}}{dt} = F_D(\vec{V} - \vec{V}_{pr}) + \frac{\vec{g}(\rho_g - \rho)}{\rho_{pr}} \quad (7)$$

206 Where  $F_D(\vec{V} - \vec{V}_{pr}) + \frac{\vec{g}(\rho_{pr} - \rho)}{\rho_{pr}}$  is the drag force per unit particle mass and

$$F_D = \frac{18\mu}{\rho_{pr}d_{pr}^2} \frac{C_D Re_r}{24} \quad (8)$$

207 Here,  $\vec{V}$  is the fluid phase velocity,  $\vec{V}_{pr}$  is the particle velocity,  $\mu$  is the molecular viscosity of the fluid,  
 208  $\rho_{pr}$  is the density and  $d_{pr}$  is the diameter of the particle.  $Re_r$  is the relative Reynolds number, it is  
 209 defined as:

$$Re_r = \frac{\rho d_p |\vec{V}_{pr} - \vec{V}|}{\mu} \quad (9)$$

210  $C_D$  is the drag coefficient; according to Morsi and Alexander model (Morsi & Alexander, 1972), it is  
 211 defined as:

$$C_D = a_1 + \frac{a_2}{Re} + \frac{a_3}{Re^2} \quad (10)$$

212 Where  $a_1$ ,  $a_2$  and  $a_3$  are defined as:

$$a_1, a_2, a_3 = \begin{cases} 0, 24, 0 & 0 < Re < 0.1 \\ 3.690, 22.73, 0.0903 & 0.1 < Re < 1 \\ 1.222, 29.1667, -3.8889 & 1 < Re < 10 \\ 0.6167, 46.50, -116.67 & 10 < Re < 100 \\ 0.3644, 98.33, -2778 & 100 < Re < 1000 \\ 0.357, 148.62, -47500 & 1000 < Re < 5000 \\ 0.46, -490.546, 578700 & 5000 < Re < 10000 \\ 0.5191, -1662.5, 5416700 & Re > 10000 \end{cases} \quad (11)$$

213

214 The heat balance to relate particle temperature to convective heat transfer at the droplet/particle  
 215 surface is modeled by following equation:

$$m_{pr} c_{pr} \frac{dT_{pr}}{dt} = h A_{r_{pr}} (T_{\infty} - T_{pr}) \quad (12)$$

216 where  $m_{pr}$  is the mass of the particle,  $c_{pr}$  is the heat capacity of the particle,  $A_{r_{pr}}$  is the surface area  
 217 of the particle,  $T_{\infty}$  is the local temperature of the continuous phase and  $h$  is the convective heat  
 218 transfer coefficient. The convective heat transfer coefficient is evaluated using the correlation of  
 219 Ranz and Masrshall (Ranz & Marshall, 1952 a) and (Ranz & Marshall, 1952 b) as:

$$\frac{hd_p}{k_{\infty}} = 2.0 + 0.6Re_r^{1/2} Pr^{1/3} \quad (13)$$

220 Here  $k_{\infty}$  is the thermal conductivity and  $Pr (c_p \mu / k_{\infty})$  is the Prandtl number of the continuous  
 221 phase

222 Turbulence Modeling

223 Scale resolving technique is adopted to resolve larger eddies through Wall Modeled LES (WMLES)  
 224 Model. As Reynolds number increases and the boundary layer become thinner, the size of important  
 225 energy bearing eddies decreases. In Large Eddy Simulations (LES), the important energy bearing

226 eddies must be resolved, thus the cost of maintaining grid resolution becomes prohibitive while  
 227 much smaller time steps are also required. A promising approach to overcome the Reynolds number  
 228 scaling limitation of LES is the algebraic Wall-Modeled LES approach. In this model larger eddies are  
 229 resolved while eddies in thinner near-wall regions; in which the wall distance is much smaller than  
 230 the boundary-layer thickness but it is still potentially very large in wall units (Piomelli & Balaras,  
 231 2002), is modeled with RANS, hence considerably reducing the computational cost. Gaussian filter is  
 232 applied to filter out eddies based on the length scale  $\Delta$  (Shur, et al., 2008).

$$\bar{\phi}(x, t) = \int_D \phi(x', t) G(x, x', \Delta) dx' \quad (14)$$

$$\Delta = \min(\max(C_w \cdot ds_w; C_w \cdot h_{max}, h_{wn}); h_{max}) \quad (15)$$

233  $h_{max}$ = maximum edge length,  $h_{wn}$ = grid step in wall-normal direction,  $C_w=0.15$ ,  $d_w$ = distance from  
 234 wall.

235 After putting the filtered out variables in Navier-Stokes equation and rearranging the terms, it could  
 236 be expressed as:

$$\frac{(\partial \bar{V}_i)}{\partial t} + \frac{\partial (p \bar{V}_i \bar{V}_j)}{\partial x_j} = -\frac{\partial \bar{P}}{\partial x_i} + \frac{\partial (\tau_{ij} + \tau_{ij}^s)}{\partial x_j} \quad (16)$$

237 This equation could be resolved except of the subgrid-scale stress  $\tau_{ij}^s$ . It can be expressed by the  
 238 Boussinesq hypothesis (Hinze, 1975) as:

$$\tau_{ij}^s - \frac{1}{3} \tau_{kk} \delta_{ij} = -2\mu_t S_{ij} \quad (17)$$

239 The subgrid scale eddy viscosity is modeled with the Smagorinsky SGS model (Smagorinsky, 1963),  
 240 the van Driest damping (Van Driest, 1956) and mixing length model as:

$$\nu_t = \min \left[ (k ds_w)^2, (C_{smag} \Delta)^2 \right] \left[ 1 - \exp[-(y^+/25)^3] \right] |S - \Omega| \quad (18)$$

241  $C_{smag} = 0.2$  is the Smagorinsky constant, as established by Shur et al (Shur, et al., 1999),  $\Omega$ = is the  
 242 vorticity,  $S$  is the magnitude of the strain tensor,  $k = 0.41$  is the Von Karman Constant.

## 243 Test Case Simulated

244 Figure 2 depicts the geometry used in the simulations. The figure is not drawn according to scale. The  
245 working fluids are superheated steam and light fuel oil. The liquid port has diameter ( $d_l$ ) 2.1 mm and  
246 length ( $l_l$ ) 30 mm. The gas port has diameter ( $d_g$ ) 1.6 mm and length ( $l_g$ ) 4 mm. Both the mixing  
247 port and the premixed zone has diameter 2.6 mm and lengths 12.4 mm and 5.6 mm respectively.  
248 The angle between the fuel port and the mixing port is 42.5°. The pressure and temperature  
249 conditions at the inlet of the fuel port are 20°C and 19 bars, and at the inlet of steam port are 210 °C  
250 and 11 bars respectively. The density and kinematic viscosity of the light fuel oil are 0.93 kg/m<sup>3</sup> and  
251 4,1 mm<sup>2</sup>/s respectively, while steam is modeled as ideal gas. The condition at the outlet of  
252 simulation zone is air at 1 bar and room temperature. The Sauter mean diameters (SMD) of the  
253 droplets are measured on each 3 mm slot on the plane A along the Y axis as shown in Figure 2. Plane  
254 A is located at the distance of 32 mm from the nozzle orifice. This distance is chosen on the basis of  
255 computational affordability. The geometry is meshed in ANSYS Meshing with polyhedral grid.  
256 Dynamic solution-adaptive mesh refinement in ANSYS Fluent is used to dynamically adapt the mesh  
257 at the gas-liquid interface in the VOF simulations through polyhedral unstructured mesh adaption  
258 (PUMA) method. This adaptation travels with the gas-liquid interface and the number of the cells  
259 changes with the flow, once liquid lumps are converted into the DPM particles; coarser grid is used to  
260 track the particles. This method significantly reduces the mesh count. Three levels of dynamic mesh  
261 refinement are used while the minimum cell volume is set to the order of 10<sup>-16</sup> m<sup>3</sup>. The minimum  
262 cell volume is chosen based on the droplet size distribution to avoid over-refinement of the grid in  
263 order to run the simulations more efficiently. A grid independent study is conducted with a minimum  
264 cell volume of 10<sup>-16</sup> m<sup>3</sup> and 10<sup>-17</sup> m<sup>3</sup> (equivalent cubic cell size of ~5 and ~3μm, respectively).  
265 The results are displayed in the appendix I (Figure 9 and Figure 10). It can be seen in Figure 9 that the  
266 drop size distribution and in Figure 10 that the average volume fraction of the light fuel oil over one  
267 hundred thousand time steps are almost the same for both meshes. Figure 3 shows an instantaneous

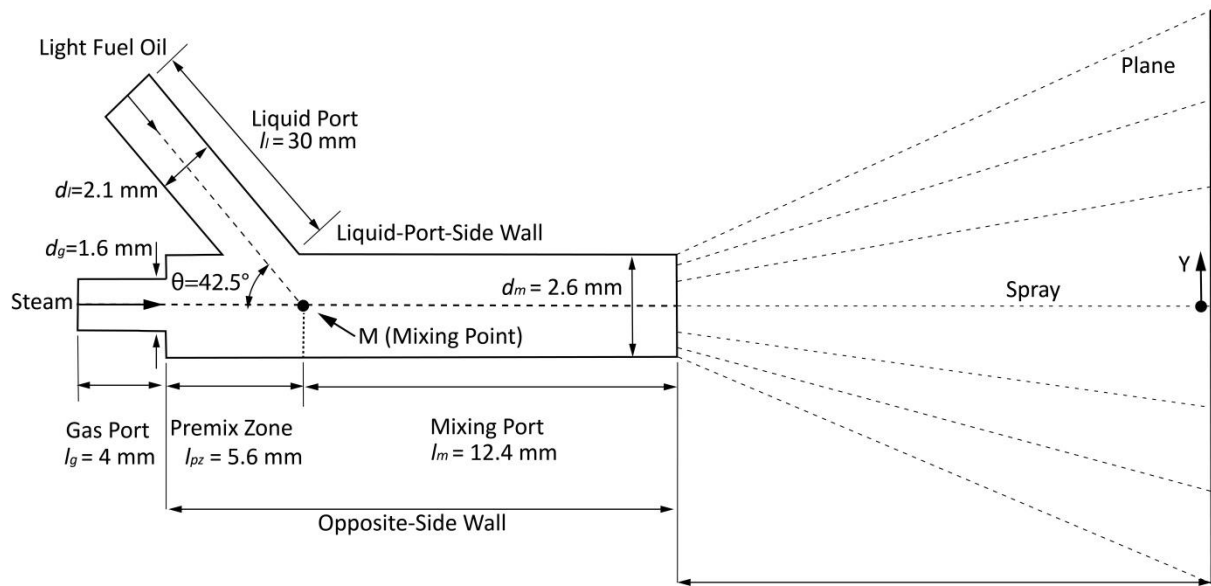


268 picture of numerical grid; it can be seen that the mesh is refined around gas-liquid interface. Mass  
269 flow inlet boundary conditions are used for the inlets and pressure outlet boundary condition is used  
270 for the outlet. In the first set of the simulations the mass flow rate of the steam is kept constant at  
271 0.00400 *kg/s* while the mass flow rate of fuel oil is varied from 0.1329 *kg/s* to .38 *kg/s* ; the  
272 corresponding values of steam-to-fuel oil mass flow rate ratios are from 0.01053 to 0.0301  
273 respectively. In the second set of simulations, the mass flow rate of the steam is kept constant at  
274 0.0005 *kg/s* while the mass flow rate of the fuel oil is varied from 0.005 *kg/s* to 0.0167 *kg/s* ; the  
275 corresponding steam-to-fuel oil mass flow rate ratios are from 0.03 to 0.1 respectively. The Reynold  
276 numbers for the flow conditions simulated are between 10,000 and 13,000. They are calculated from  
277 the following expression:

$$Re = \frac{\rho_{mix,M} V_r d_m}{\mu} \quad (19)$$

278 Here  $\rho_{mix,M}$  is the average mixture density of the gas and liquid at the mixing point,  $V_r$  is the relative  
279 velocity between gas and liquid phase, and  $d_m$  is the mixing port diameter.

280 The asphericity value for the VOF-to-DPM transition mechanism is initially set to the value of 0.01. As  
281 the flow is developed in the mixing port of the atomizer, it is changed to the value of 2.5 to track the  
282 droplets and measure its SMD.



283

284 Figure 2: Geometry of twin-fluid Y-jet atomizer used in the simulation and schematic explanation of the subsequent spray  
 285 formation.

286

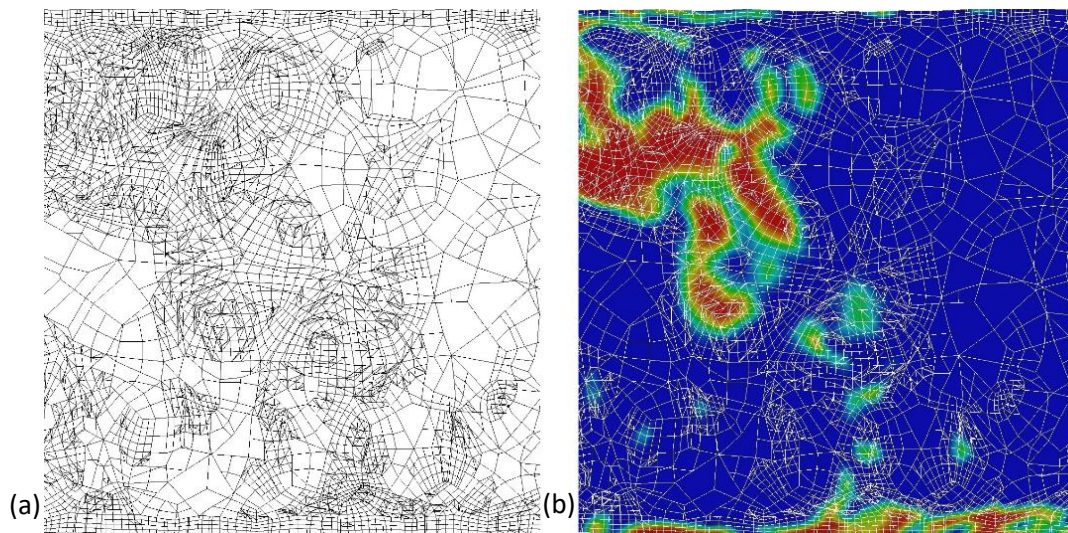
287

288

289

290

291



292

Figure 3 (a) Instantaneous grid (b) Instantaneous grid with super imposed volume fraction of light fuel oil.

293

294

295

## 296 Results & Discussion

297 Visualization of the simulation results has been carried out to analyze the internal flow behavior

298 within the mixing-port of the twin-fluid Y-jet atomizer. Figure 4 show the internal flow patterns

299 within the mixing-port of atomizer for two different steam mass flow rates and various oil mass flow

300 rates. For a reference, a schematic of the mixing-port at the same scale is drawn at the top of Figure

301 3. The red colour depicts the volume fraction of fuel oil to be 1 while blue colour depicts the volume

302 fraction of the fuel oil to be zero i.e. the volume fraction of the steam as 1. The instability of the  
303 liquid jet emanating from the liquid port into the mixing port is amplified by the impingement of high  
304 velocity gas stream; leading to the creation of smaller liquid ligaments and sheets. This phenomenon  
305 could be explained by the shear action of the gas stream and by the wave lengths that grow on the  
306 surface of the liquid jet/column, which are affected by surface tension, aerodynamic and viscous  
307 forces (Dombrowski & Johns, 1963). The high relative velocity of the gas helps the dispersion of the  
308 liquid and delays or minimise the chances of droplet coalescence (Pacifico & Yanagihara, 2014).

309 At first, it can be realized from the contours in the Figure 4 that both  $M_l$  and  $M_g$  clearly influence the  
310 oil film formation within the mixing port. The amount of oil stream crossing the mixing port increases  
311 with a decrease of  $M_g$  and/or an increase of  $M_l$ , and forms a thicker oil film at the opposite side wall.  
312 The internal flow pattern far downstream of the mixing point becomes an annular-mist flow with  
313 asymmetrical film thickness along the wall of the mixing-port, as characterized by Mullinger and  
314 Chigier (Mullinger & Chigier, 1974), Andreussi et al. (Andreussi, et al., 1994), (Andreussi, et al., 1992),  
315 Pacifico and Yanagihara (Pacifico & Yanagihara, 2014) Mlkvik et al. (Mlkvik, et al., 2015) and Nazeer  
316 et al. (Nazeer, et al., 2019). The rate of direct drop formation within the mixing port is also strongly  
317 dependent on both  $M_g$  and  $M_l$ . That is, the number of drop increases with an increase in  $M_l$  and/or  
318  $M_g$  (Song & Lee, 1996).

319 On the same figure, the values of the gas-to-liquid mass flow rate ratio ( $M_g/M_l$ ) and the liquid-to-gas  
320 momentum ratio ( $\varphi$ ) are also shown. These parameters are already adopted in the studies (Neya, et  
321 al., 1975), (De Michele, et al., 1991), (Andreussi, et al., 1992), (Song & Lee, 1994), (Andreussi, et al.,  
322 1994), (Pacifico & Yanagihara, 2014), (Mlkvik, et al., 2015) and (Nazeer, et al., 2019). Here  $\varphi$  is  
323 defined as:

$$\varphi = \frac{G_l^2 d_l^2 \rho_g M}{G_g^2 d_m^2 \rho_l} \sin \theta \quad (20)$$

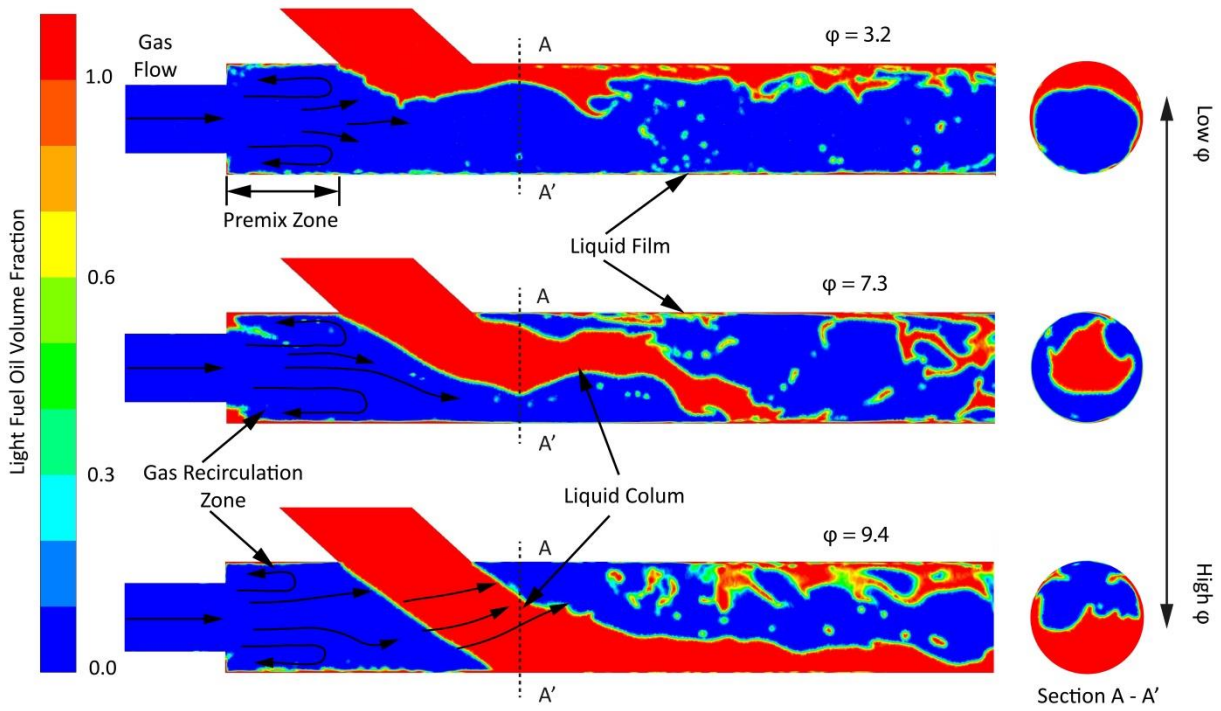
324 Where “ $G$ ” is the mass velocity, “ $\rho$ ” is the density, “ $d_m$ ” is the mixing port diameter and “ $\theta$ ” is the  
325 angle between liquid and gas ports. The indices “ $g$ ” and “ $l$ ” denote the gas and liquid respectively;  
326  $\rho_{gM}$  is the density of the steam at the mixing point.

327 From Figure 4 one can point out that when the gas flow rates are different while  $M_g/M_l$  is kept  
328 constant (see Figures 4a and 4i), the flow pattern appears to be much different. In fact, when  
329 momentum ratios are near to each other, for instance (4a and 4f) and (4h and 4c) flow development  
330 looks very similar. Thus, from the above observations, the liquid-to-gas momentum ratio ( $\varphi$ ) seems  
331 to be a better dimensionless parameter to explain the internal flow pattern than the gas-to-liquid  
332 mass flow rate ratio. Song and Lee (Song & Lee, 1996) also reached to the conclusion that  
333 momentum ratio is a better parameter to describe the internal flow pattern.

334 Figure 5 helps to explain the variation in gas and liquid flow patterns within the mixing port of Y-jet  
335 nozzle based on the momentum ratio. The contours of the volume fraction of light fuel oil are  
336 displayed for the liquid-to-gas momentum ratios of 3.2, 7.3 and 9.4. When the liquid-to-gas  
337 momentum ratio is low (say  $\varphi < 7$ , Figures 4a, 4e, 4f and 4g), most of the liquid forms thick film at  
338 liquid-port-side wall of the mixing port. This is because the gas jet momentum dominates and liquid  
339 stream cannot penetrate into the mixing-port easily. Due to this, the main stream of the gas tends to  
340 be deflected towards the opposite side wall by the liquid film and thus, a large recirculation appears  
341 in the premix zone. Hence, a portion of the liquid stream flows in a film shape toward the upstream  
342 by recirculating gas. For example the liquid film in the upper left corner of Figures 4b, 4f, 4g and 4i  
343 clearly indicates the reverse flow of the liquid film by strong recirculation of the gas. As the main gas  
344 stream at the exit of the gas port meets the reverse flow, it disintegrates in to small droplets and  
345 flows downstream along the core, as it can be seen in Figure 6. At the same time, as it can be seen in  
346 Figures 4a, 4e, 4f and 4g, droplets are also entrained from the main liquid film, flowing downstream.

347





350

351 Figure 5 Illustration of internal flow pattern based on liquid-to-gas momentum ratio.

352

353 When the liquid-to-gas momentum ratio increases (for  $7 < \phi < 9$ , Figures 4b, 4c and 4h), the liquid  
354 jet penetrates into the center of the mixing port and starts to blocking the path of the flowing gas  
355 ensuing from the gas port; this leads to deflection of the gas stream towards the opposite side wall.  
356 This is denoted as blockage effect (Mullinger & Chigier, 1974). Thus, a substantial amount of liquid  
357 film at the opposite side is entrained into the gas core by the highly deflected gas stream while the  
358 rate of the entertainment increases with the amount of gas stream deflection. The number of  
359 droplets formed around the mixing point from the liquid column increases with increasing  
360 penetration depth of liquid, since the interfacial area between the gas and liquid increases. The liquid  
361 jet in this regime is unstable and gradually breaks up as a result of imbalance between surface forces,  
362 velocity fluctuations, pressure fluctuations and steep velocity gradients. This leads to temporally  
363 fluctuating liquid sheet/film formation within in the mixing-port, just before the orifice exit (Figures  
364 4b and 4h).

365 As the liquid-to-gas momentum ratio increases further ( $\varphi > 9$ , Figures 4d and 4i), part of the liquid  
366 jet reaches the opposite wall and the liquid film thickness at both sides of the mixing port becomes  
367 similar in thickness. If the liquid-to-gas momentum ratio increases further, the liquid jet completely  
368 reaches the opposite side wall and the film thickness at the opposite side wall becomes thicker than  
369 the liquid-port-side wall, as can be seen in the Figure 4d. With this condition, the blockage effect  
370 becomes more prominent because the gas stream has to flow around the liquid jet crossing the  
371 mixing point. Due to the high shear of the gas flow, thin sheets of the liquid are extracted from the  
372 liquid jet around the mixing point (liquid-port-side wall Figures 4d and 4i). These sheets are further

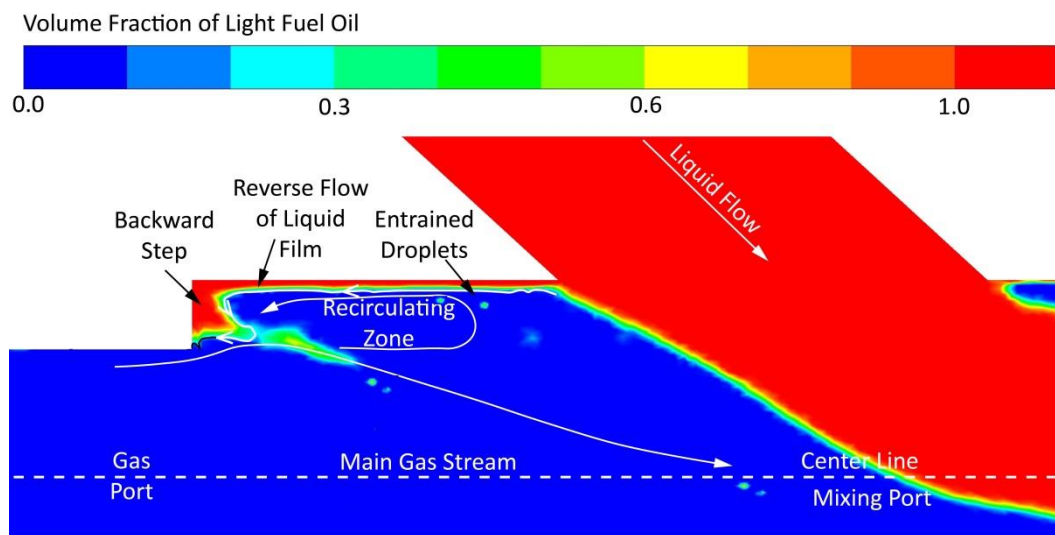


Figure 6 Illustration of the recirculating flow in the premix zone of the mixing port of the atomizer.

373 broken down into smaller droplets in the downstream flow. The quantity of these liquid sheet  
374 formations increases with the deeper penetration of the liquid jet or with greater gas flow rate.

375

376

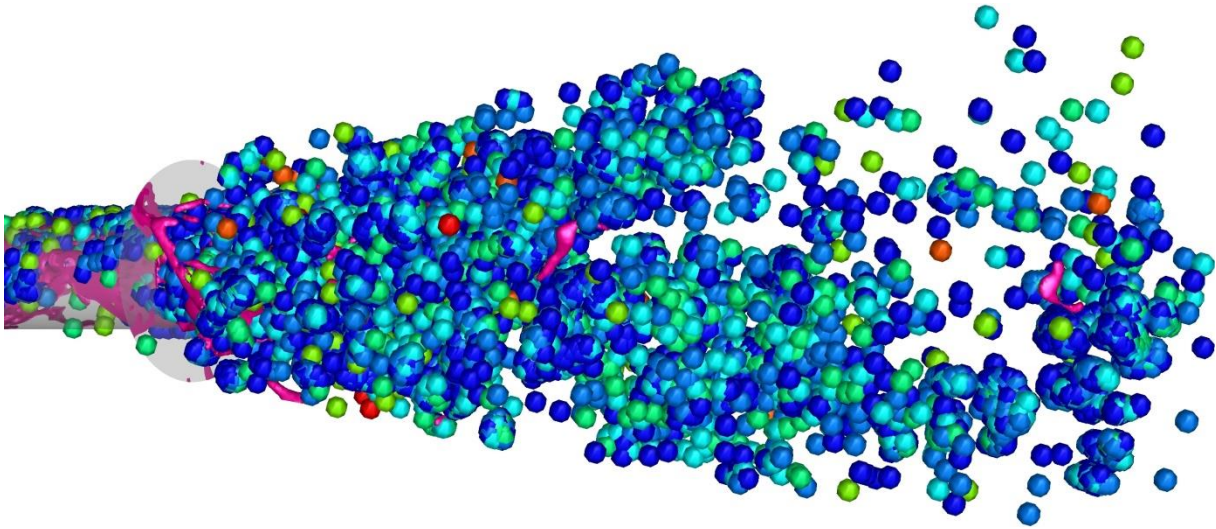


Figure 7 Spray formation by internally mixing twin-fluid Y-jet atomizer at the flow time of 0.0006 s for the liquid-to-gas momentum ratio of 7.3. The magenta colored blobs and ligaments represent the liquid resolved by VOF formulations and spherical particle represents the liquid droplets tracked by DPM model.

378 Figure 7 shows the spray formation process of internally mixing twin-fluid Y-jet atomizer. The  
 379 magenta colored blobs and ligaments depict the resolved liquid by the VOF method. Once the  
 380 specified criteria of asphericity are satisfied, the resolved liquid is turned into discrete droplets, as  
 381 represented by the spherical particles in Figure 7. Figure 8 shows the Sauter Mean Diameter (SMD)  
 382 drop size distribution for various liquid-to-gas momentum ratios measured on the plane A along the  
 383 Y axis as indicated in Figure 2. The droplet size distribution is strongly affected by the internal flow  
 384 pattern and the initial atomization within the mixing port of the nozzle, as explained earlier. That is,  
 385 the small droplets at the center are forming from the core flow within the mixing port of the  
 386 atomizer, whereas the larger droplets at both sides are forming from the annular liquid film present  
 387 on the walls of the mixing port. It can be also noticed that as the momentum ratio increases, the  
 388 peak value of the Sauter Mean Diameter in the positive Y axis decreases, indicating that the liquid  
 389 film thickness at the liquid-port-side wall of the mixing port decreases, due to easier penetration of  
 390 the liquid column into the gas stream. When the momentum ratio is less than 5.4 (Figures 8a, 8b and  
 391 8c), the values of SMD in the negative Y axis changes slightly with the increasing momentum ratios.  
 392 This is because the liquid column does not have enough momentum to reach the opposite side wall.  
 393 However, as the liquid-to-gas momentum ratio increases further than that, the values of SMD in the



394 negative Y axis become sufficiently large and the distribution becomes somewhat symmetrical  
395 (Figure 8d). If  $\varphi$  increases further, the momentum of the liquid column dominates and hence the  
396 values of SMD in the negative Y axis become larger than the values in positive Y axis; the curve again  
397 shows asymmetrical shapes. At extremely high values of momentum ratio (Figure 8h), a sudden  
398 decrease in the values of SMD in the positive Y axis is observed. This is due to the shear-induced  
399 breakup caused by the increased blockage effect (Figure 4h). These distributions agree well with the  
400 film thickness variation within the mixing port measured by Andreussi et al. (Andreussi, et al., 1994)  
401 and the drop size distribution measured by (Song & Lee, 1996).

402

403

404

405

406

407

408

409

410

411

412

413

414

415

416

417

418

419

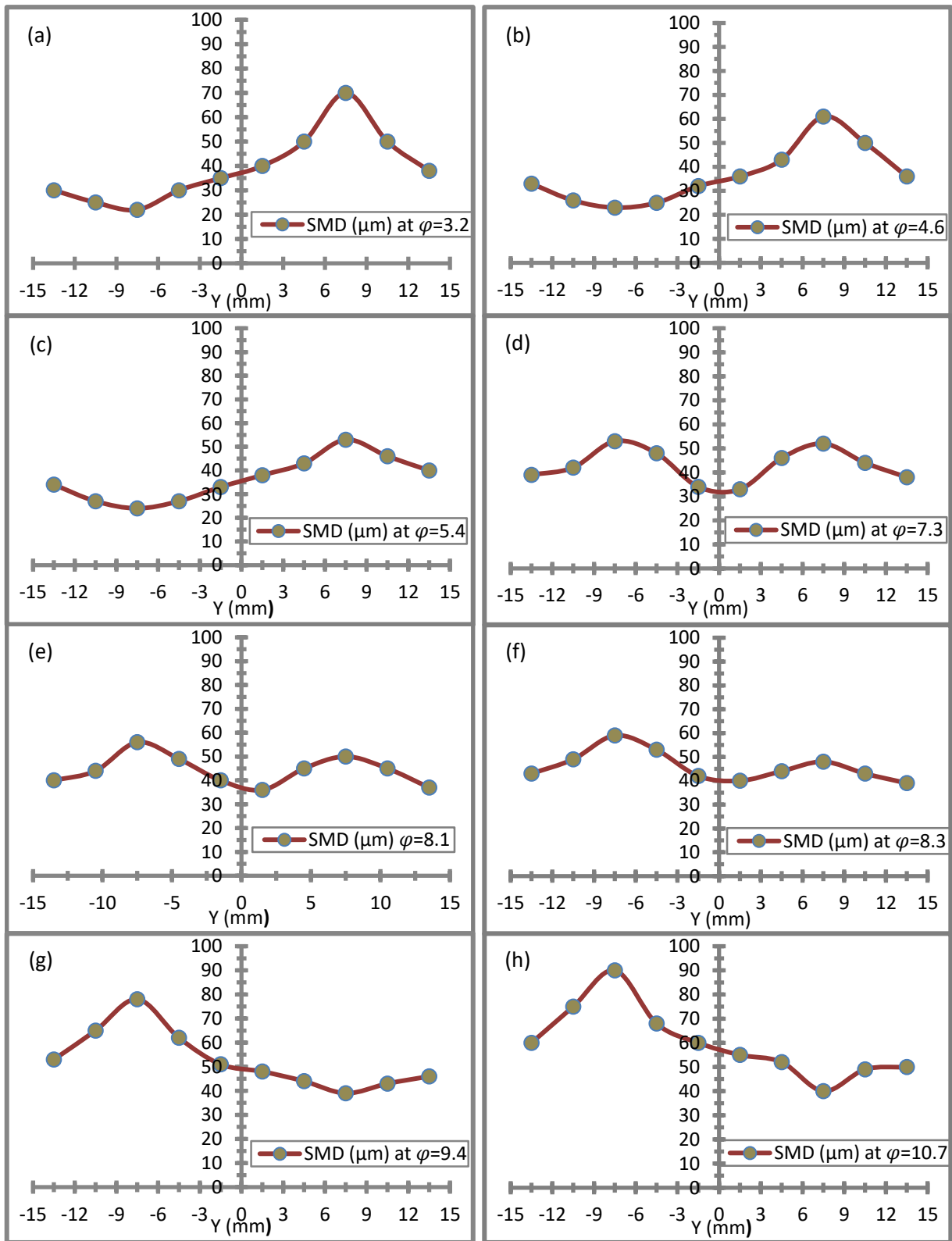


Figure 8 Sauter mean diameter drop size distribution for the liquid-to-gas momentum ratios of (a) 3.2, (b) 4.6, (c) 5.4, (d) 7.3, (e) 8.1, (f) 8.3, (g) 9.4 and (h) 10.7.

432

433

## 434 Conclusion

435 Simulation results have been presented for the internal flow behavior and the atomization  
436 mechanism of internally mixing twin-fluid Y-jet atomizers. Working fluids were super-heated steam  
437 and light fuel oil. The multiphase flow was modeled by hybrid Eulerian-Eulerian and Eulerian-  
438 Lagrangian approach through VOF-to-DPM transition mechanism. Adaptive mesh refinement was  
439 used to resolve the gas-liquid interface on the fine mesh required by the VOF formulations. When  
440 the criteria of asphericity were satisfied, discrete droplets were tracked on the coarser mesh through  
441 DPM model. A hybrid RANS and LES technique, i.e. WMLES (wall modeled large eddy simulations)  
442 was used to resolve the larger eddies with LES formulations, while smaller eddies were modeled with  
443 the Prandtl length model. Two dimensionless parameters namely, gas-to-liquid mass flow rate ratio  
444 and the liquid-to-gas momentum ratio have been investigated; the latter is considered to be a more  
445 representative dimensionless parameter to describe the internal flow behavior and spray  
446 characteristics. The variation in the internal flow pattern, characterized by the penetration of the  
447 liquid column into the gas core and the film flow within the mixing port could be effectively  
448 explained by the liquid-to-gas momentum ratio. The simulations have confirmed that variation in the  
449 circumferential liquid film thickness within the mixing port coincides well with the spatial distribution  
450 of the droplets outside the atomizer. Moreover, the variation in the droplet SMD distribution over  
451 the Y direction as the function of the liquid-to-gas momentum ratio, agrees well with the mean film  
452 thickness and drop size distribution reported previously in the open literature, except for the sharp  
453 decrease in the SMD in the positive Y direction at extremely high liquid-to-gas momentum ratios.

## 454 Data Availability Statement

455 ANSYS Fluent case and data files of the simulations that support the findings of this study  
456 are available from the corresponding author upon reasonable request.

## 457 Acknowledgements

458 The project has received funding from European Union Horizon-2020 Research and Innovation  
459 MSCA-ITN Programme with acronym HAOS: Grant Agreement No. 675676.

## 460 References

- 461 Andreussi, P. et al., 1994. *Measurement of Film Thickness within a Y-Jet Atomizer*. s.l., International  
462 conference on liquid atomization and spray systems, pp. 632-639.
- 463 Andreussi, P., Tognotti, L., Michele, G. D. & Graziadio, M., 1992. Design and Characterization of Twin-  
464 Fluid Y-Jet Atomizers. *Atomization and Sprays*, Volume 2, pp. 45-59.
- 465 Arcoumanis, C., Gavaises, M., Argueyrolles, B. & Galzin, F., 1999. Modeling of Pressure-Swirl  
466 Atomizers for GDI Engines. *Transactions Journal of Engines, SAE Paper*, 108(3), pp. 516-532.
- 467 Barreras, F., Lozano, A., Ferreira, G. & Lincheta, 2008. *The effect on the inner flow on the performance*  
468 *of a twin-fluid nozzle with an internal mixing chamber*. Como Lake, European Conference on Liquid  
469 Atomization and Spray Systems.
- 470 Barreras, F., Lozano, A., Ferreira, G. & Lincheta, E., 2006. *Study of the Internal Flow Condition on the*  
471 *Behavior of Twin-Fluid Nozzle with Internal Mixing Chamber*. Kyoto, International Conference on  
472 Liquid Atomization and Spray Systems.
- 473 Brackbill, J. U., Kothe, D. B. & Zemach, C., 1992. A continuum method for modeling surface tension..  
474 *Journal of Computational Physics*, 100(2), pp. 335-354.
- 475 Buckner, H. N., Sojka, P. E. & Lefebvre, A. H., 1990a. Effervescent atomization of coal-water slurries.  
476 *ASME publication*, Volume 30, pp. 105-108.
- 477 Buckner, H. N., Sojka, P. E. & Lefebvre, A. H., 1990b. *Effervescent atomization of non-Newtonian*  
478 *single phase liquid*. Hartford, Connecticut, Proceedings of the fourth Annual Conference on  
479 Atomization and Sprays.
- 480 De Michele, G., Graziadio, M., Morelli, F. & Novelli, G., 1991. *Characterization of the spray structure*  
481 *of a large scale H.F.O. Atomizer*. Gaithersburg, Proceedings of ICLASS.
- 482 Dombrowski, N. & Johns, W. R., 1963. The aerodynamic instability and disintegration of viscous liquid  
483 sheets. *Chemical Engineering Science*, 18(3), pp. 203-214.
- 484 Gavaises, M. & Arcoumanis, C., 2001. Modelling of sprays from high-pressure swirl atomizers.  
485 *International Journal of Engine Reserach*, 2(2), pp. 95-117.
- 486 Hinze, J. O., 1975. *Turbulence*. New York: McGraw-Hill Publishing Co..
- 487 Hirt, C. W. & Nichlos, B. D., 1981. Volume of fluid (VOF) method for the dynamics of free boundaries.  
488 *Journal of Computational Physics*, 39(1), pp. 201-225.
- 489 Inamura, T. et al., 2019. Effects of prefilmer edge thickness on spray characteristics in prefilming  
490 airblast atomization. *International Journal of Multiphase Flow*, Volume 121.
- 491 Jiang, X., Siamas, G. A., Jagus, K. & Karayiannis, T. G., 2010. Physical modelling and advanced  
492 simulations of gas-liquid two-phase jet flows in atomization and sprays. *Progress in Energy and*  
493 *Combustion Science*, Volume 36, pp. 131-167.

494 Kufferath, A., Wende, B. & Leuckel, W., 1999. Influence of liquid flow conditions on spray  
495 characteristics of internal-mixing twin-fluid atomizers. *International journal of heat and fluid flow*,  
496 Volume 20, pp. 513-519.

497 Kumar, V. et al., 2018. *A hybrid approach for modeling fully resolved liquid film formation by*  
498 *converting lagrangian particles to eulerian VOF structures*. Chicago, International Conference on  
499 Liquid Atomization and Sprays Systems.

500 Lefebvre, A. H., 1992. Twin-Fluid Atomization: Factors Influencing Mean Drop Size. *Atomization and*  
501 *Sprays*, Volume 2, pp. 101-119.

502 Lefebvre, A. H., 1980. Airblast Atomization. *Progress in Energy and Combustion Sciences*, Volume 6,  
503 pp. 223-261.

504 Li, H., Rutland, C. J., Perez, F. E. H. & Im, G. H., 2020. Large-eddy spray simulation under direct-  
505 injection spark-ignition engine-like conditions with an integrated atomization/breakup model.  
506 *International Journal of Engine Research*.

507 Li, Z. et al., 2012. Mixing and atomization characteristics in an internal-mixing twin-fluid atomizer.  
508 *Fuel*, Volume 97, pp. 306-314.

509 Mlkvik, M. et al., 2015. Twin-Fluid atomization of viscous liquids: The Effect of atomizer construction  
510 on breakup process, spray stability and droplet size. *International Journal of Multiphase*, Volume 77,  
511 pp. 19-32.

512 Morsi, S. A. & Alexander, A. J., 1972. An investigation of Particle Trajectories in Two-Phase Flow  
513 Systems. *Journal of Fluid Mechanics*, 55(2), pp. 193-208.

514 Mullinger, P. & Chigier, N., 1974. The Design and Performance of Internal Mixing Multijet Twin Fluid  
515 Atomizers. *Journal of the institute fuel*, Volume 47, pp. 251-261.

516 Nazeer, Y. H., Ehmann, M., Koukouvinis, P. & Gavaises, M., 2019. The Influence of Geometrical and  
517 Operational Parameters on Internal Flow Characteristics of Internally Mixing Twin-Fluid Y-Jet  
518 Atomizers. *Atomizations & Sprays*, 59(5), pp. 403-428.

519 Neya, K., Sato, S. & Hatopri, K., 1975. Study of y-jet Twin Fluid Atomizer. *Ship Reserach Institute*, 12(1),  
520 pp. 1-19.

521 Nykteri, G. et al., 2020. A  $\Sigma$ - $\Upsilon$  two-fluid model with dynamic local topology detection: Application to  
522 high-speed droplet impact. *Journal of Computational Physics*, Volume 408.

523 Okabe, T. et al., 2019. Time-dependent breakup length of liquid sheet in prefilming type of airblast  
524 atomizer. *Atomization & Sprays*, 29(1), pp. 289-303.

525 Pacifico, A. L. & Yanagihara, J. I., 2014. The influence of geometrical and operational parametrs on Y-  
526 jet atomizers performance. *Journal of Brazilian Society of Mechanical Science and Engineering*,  
527 Volume 36, pp. 13-32.

528 Piomelli, U. & Balaras, E., 2002. Wall-layer Models for Large-Eddy Simulations. *Annual Review of Fluid*  
529 *Mechanics*, Volume 34, pp. 349-374.

530 Prasad, K. S. L., 1982. *Characterization of Air Blast Atomizers*. madison wisconsin, International  
531 Conference on Liquid Atomization and Spray Systems.

532 Ranz, W. E. & Marshall, W. R., 1952 a. Evaporation from drops, Part 1. *Chemical Engineering*  
533 *Progress*, 48(3), pp. 141-146.

534 Ranz, W. E. & Marshall, W. R., 1952 b. Evaporation from Drops Part 1 and Part 2. *Chemical*  
535 *Engineering Progress*, 48(4), pp. 173-180.

536 Roesler, T. C. & Lefebvre, A. H., 1989. Studies on aerated-liquid atomization. *International journal of*  
537 *turbojet engines*, Volume 6, pp. 221-230.

538 Roudini, M. & Wozniak, G., 2018. Experimental Investigation of Spray Characteristics of Pre-Filming  
539 Air-blast Atomizers. *Journal of Applied Fluid Mechanics*, 11(6), pp. 1455-1469.

540 Sami, M., Schuetze, P., Hutcheson, P. & Aguado, P., 2019. *Best Practices in the numerical modelling of*  
541 *liquid atomization processes*. Tempe, Arizona, ILASS-Americas 30th Annual Conference on Liquid  
542 Atomization and Spray System.

543 Schtze, J. et al., 2018. *A multimodel hybrid approach for the numerical simulation of fluid phase*  
544 *dispersion process*. Chicago, International Conference on Liquid Atomization and Sprays Systems.

545 Shur, M. L., Spalart, P. R., Strelets, M. K. & Travin, A. K., 2008. A hybrid RANS-LES approach with  
546 delayed-DES and wall-modelled LES capabilities. *International Journal of Heat and Fluid Flow*, Volume  
547 29, pp. 1638-1649.

548 Shur, M., Strelets, P., Spalart, M. & Travin, A., 1999. Detached-eddy simulation of an airfoil at high  
549 angle of attack. *Engineering Turbulence Modeling and Measurements*, Volume 4, pp. 669-678.

550 Smagorinsky, J., 1963. General Circulation Experiments with the Primitive Equations. *Monthly*  
551 *Weather Review*, Volume 91, pp. 99-165.

552 Song, S. H. & Lee, S. Y., 1996. Study of Atomization Mechanism of Gas/Liquid Mixtures Flowing  
553 Through Y-Jet Atomizers. *Atomization and Sprays*, Volume 6, pp. 193-209.

554 Song, S. & Lee, S., 1994. *An Examination of Spraying Performance of Y-Jet Atomizers- Effect of Mixing*  
555 *Port Length*. Rouen, International Conference on Liquid Atomization and Spray Systems.

556 Sovani, S. D., Sojka, P. E. & Lefebvre, A. H., 2001. Effervescent Atomization. *Progress in Energy and*  
557 *Combustion Sciences*, Volume 27, pp. 483-521.

558 Stefanitsis, D. et al., 2019b. Numerical investigation of the aerodynamic breakup of droplets in  
559 tandem. *International Journal of Multiphase Flow*, Volume 113, pp. 289-303.

560 Stefanitsis, D., Strotos, G., Nikolopoulos, N. & Gavaises, M., 2019a. Numerical investigation of the  
561 aerodynamic breakup of a parallel moving droplet cluster. *International Journal of Multiphase Flow*,  
562 Volume 121.

563 Strotos, G. et al., 2011. Non-dimensionalisation parameters for predicting the cooling effectiveness of  
564 droplets impinging on moderate temperature solid surfaces. *International Journal of Thermal*  
565 *Sciences*, Volume 50, pp. 698-711.

566 Strotos, G., Malgarinos, I., Nikolopoulos, N. & Gavaises, M., 2016a. Aerodynamic breakup of an n-  
567 decane droplet in a high temperature gas environment. *FUEL*, Volume 185, pp. 370-380.

568 Strotos, G., Malgarinos, I., Nikolopoulos, N. & Gavaises, M., 2016b. Predicting droplet deformation  
569 and breakup for moderate Weber numbers. *International Journal of Multiphase Flow*, Volume 85, pp.  
570 96-109.

571 Strotos, G. et al., 2018. Determination of the aerodynamic droplet breakup boundaries based on a  
572 total force approach. *International Journal of Heat and Fluid Flow*, Volume 69, pp. 164-173.

573 Tonini, S., Gavaises, M. & Theodorakakos, A., 2008. Modelling of high-pressure dense diesel sprays  
574 with adaptive local grid refinement. *International journal of Heat and Fluid Flows*, Volume 29, pp.  
575 427-448.

576 Vallet, A., Burluka, A. A. & Borghi, R., 2001. Development of a Eulerian model for the 1168  
577 “atomization” of a liquid jet. *Atomization and Sprays*, 11(6).

578 Van Driest, E. R., 1956. On Turbulent flow near a wall. *Journal of Aeronautical Sciences*, Volume 23,  
579 pp. 1007-1011.

580 Zhou, X., Li, T. & Lai, Z., 2019 b. Similarity of split-injected fuel sprays for different size diesel engines.  
581 *International Journal of Engine Research*.

582 Zhou, X., li, T., Wei, Y. & Wang, N., 2019 a. Scaling liquid penetration in evaporating sprays for  
583 different size diesel engines. *International Journal of Engine Research*.

584

585

586

587

588

589

590

591

592

593

594

595

596

597

## 598 Appendix I. Grid Independent Study

599 A grid independence study was conducted to check whether the drop size distribution measured  
600 along the Y axis on the plane A change with the mesh. Two different dynamic solution-adaptive mesh  
601 refinements were used through PUMA method. Mesh "I" has three levels of dynamic mesh  
602 refinement and minimum cell volume of  $10^{-16} m^3$ , while Mesh "II" has three levels of dynamic mesh  
603 refinement and minimum cell volume of  $10^{-17} m^3$ . Average SMD distribution for the momentum  
604 ratios ( $\varphi$ ) 3.2, 7.3 and 9.4 for one hundred thousand time steps are shown in the Figure 9(a), Figure  
605 9(b) and Figure 9(c) respectively. The drop size distribution for both the meshes is almost the same.

606 Figure 10 shows the contour of the average volume fraction of the light fuel oil within the nozzle over  
607 one hundred thousand time steps for the Mesh "I" and Mesh "II" for the momentum ratios ( $\varphi$ ) of  
608 3.2, 7.3 and 9.4. The average volume fraction for both the meshes for the momentum ratios of 3.2  
609 (figure a & b), 7.3 (figure c & d) and 9.4 (figure e & f) are almost the same.

610

611

612

613

614

615

616

617

618

619



620

621

622

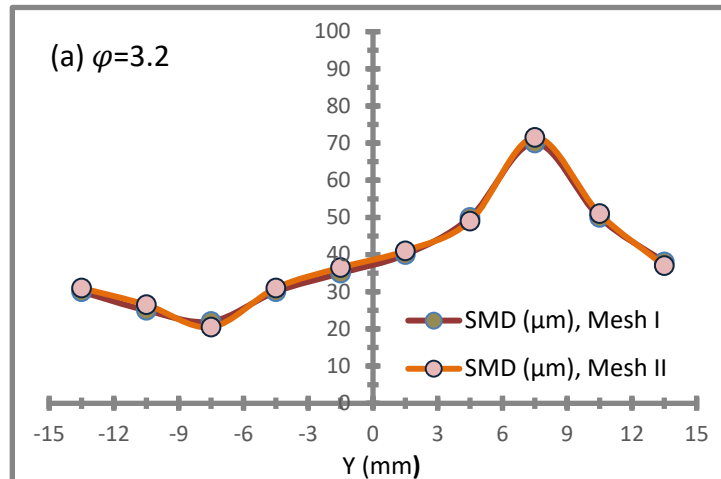
623

624

625

626

627



628

629

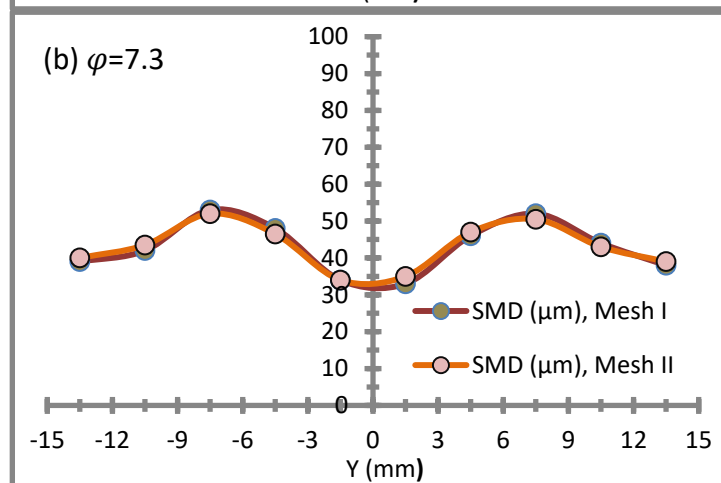
630

631

632

633

634



635

636

637

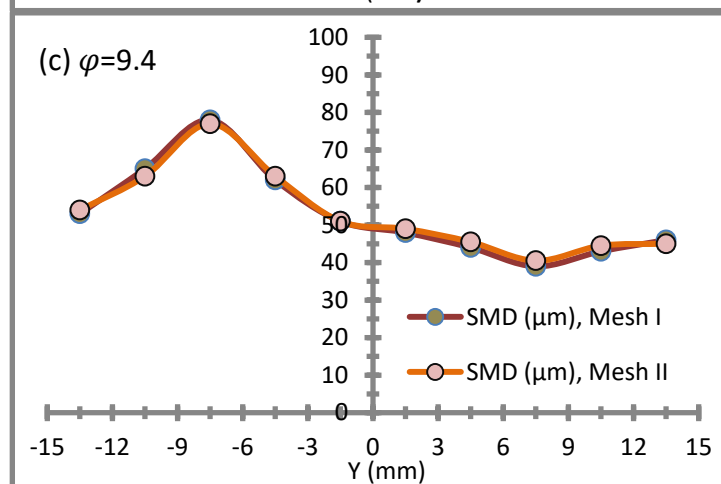
638

639

640

641

642



644

Figure 9 SMD drop size distribution for MESH I and MESH II for the liquid-to-gas momentum ratios of (a) 3.2, (b) 7.3, and (c) 9.4.

645

646

647

648

649

650  
651  
652  
653  
654  
655  
656  
657  
658  
659  
660  
661  
662  
663  
664  
665  
666  
667  
668  
669  
670  
671  
672  
673  
674  
675  
676  
677  
678  
679

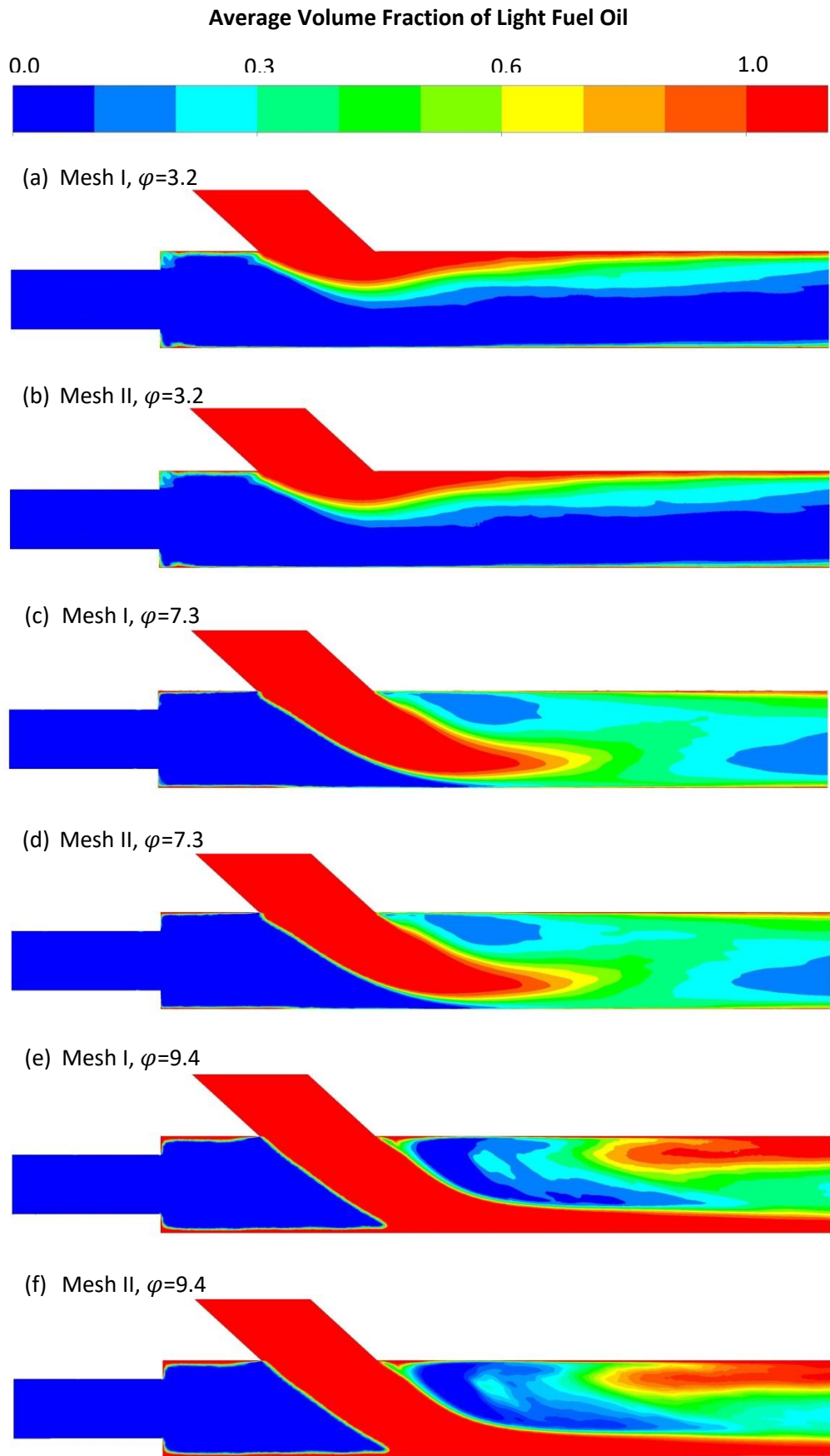


Figure 10 Average volume fraction of light fuel oil over one hundred time steps for liquid-to-gas momentum ratios of 3.2 (a) Mesh 'I' (b) Mesh 'II', 7.3 (c) Mesh 'I' (d) Mesh 'II' and 9.4 (e) Mesh 'I' (f) Mesh 'II'.

680 Appendix II. Asphericity Independent Study

681 Figure 11 shows the contour of the average volume fraction of the light fuel oil within the nozzle over  
682 one hundred thousand time steps for asphericity of 0.01 and 2.5 for the momentum ratio ( $\varphi$ ) of 2.8.  
683 The average volume fraction for both the asphericities (figure a & b) are almost the same.

684

685

686

687

688

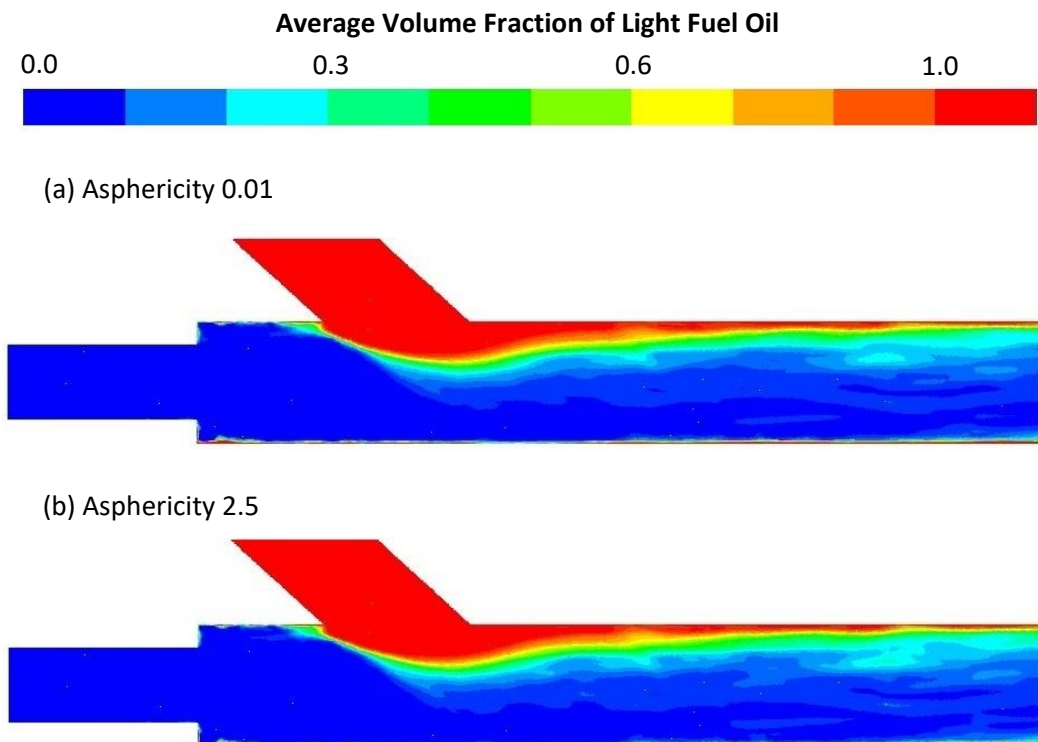


Figure 11 Average volume fraction of light fuel oil over one hundred time steps for asphericity ratios of (a) 0.01 and (b) 2.5 for the liquid-to-gas momentum ratio of 2.8.